

DOI: 10.1002/ ((please add manuscript number))

**Article type: Full Paper**

**Title** Scalable and solid-state redox functionalization of transparent single-walled carbon nanotube films for highly efficient and stable solar cells

*Kehang Cui,\* Yang Qian, Il Jeon, Anton Anisimov, Yutaka Matsuo, Esko I. Kauppinen, Shigeo Maruyama\**

Dr. K. Cui, Y. Qian, Dr. I. Jeon, Prof. Dr. Y. Matsuo, Prof. Dr. S. Maruyama  
Department of Mechanical Engineering, The University of Tokyo, Tokyo 113-8656, Japan  
E-mail: [maruyama@photon.t.u-tokyo.ac.jp](mailto:maruyama@photon.t.u-tokyo.ac.jp)

Prof. Dr. S. Maruyama

Energy NanoEngineering Laboratory, National Institute of Advanced Industrial Science and Technology (AIST), Tsukuba 305-8564, Japan

Dr. K. Cui

Current Address: Department of Mechanical Engineering, Massachusetts Institute of Technology, Cambridge, MA 02139, United States

E-mail: [cui@mit.edu](mailto:cui@mit.edu)

Prof. Dr. E. I. Kauppinen

Department of Applied Physics, Aalto University School of Science, Espoo FI-00076, Finland

Dr. A. Anisimov

Canatu Oy, Helsinki FI-00390, Finland

Keywords: solar cells, carbon nanotubes, functional coatings, doping

### **Abstract.**

This study reports a scalable and room-temperature solid-state redox functionalization process for single-walled carbon nanotubes (SWNTs) with instant efficacy and high stability. By drop-casting/spin-coating  $\text{CuCl}_2/\text{Cu}(\text{OH})_2$  colloidal ethanol solution onto SWNT films, the sheet resistance of the SWNT films achieves  $69.4 \Omega/\text{sq}$ . without noticeable increase for more than 12 months. The charge transfer mechanism between the redox and the SWNTs is revealed by Raman and X-ray photoelectron spectroscopies. The SWNT/silicon solar cells are utilized as a benchmark to evaluate the effectiveness of the redox functionalization process and its compatibility for device integration. The power conversion efficiency (PCE) of the SWNT/Si solar cell increases by 115% after redox functionalization, reaching the value of 14.09% without degradation in the ambient for over 12 months. Temperature-dependent operation characteristics of the redox functionalized SWNT/Si solar cells demonstrate that the

Fermi level unpinning and enhanced tunneling of the charge carriers contribute to the significant improvement of the photovoltage and fill factor. The  $\text{CuCl}_2/\text{Cu}(\text{OH})_2$  redox also serves as an antireflection layer, resulting in a 20% increase of the photocurrent. The proposed redox functionalized SWNTs are promising as multifunctional transparent conductive films for wide-range solar cell applications.

## 1. Introduction

Transparent conductive films (TCFs) play a key role in wide-range emerging optoelectronic and biomedical applications including solar cells,<sup>[1-4]</sup> touch panels,<sup>[5-8]</sup> light-emitting diodes (LEDs),<sup>[9-11]</sup> sensors,<sup>[12-14]</sup> *etc.* Single-walled carbon nanotube (SWNT) films are one of the potential candidates of TCFs.<sup>[15-18]</sup> Compared with other materials such as Ag nanowires (AgNWs), indium tin oxide (ITO) and conductive polymers such as poly(3,4-ethylenedioxythiophene) polystyrene sulfonate (PEDOT:PSS),<sup>[19, 20]</sup> SWNTs are mechanically flexible, chemically stable and environmentally benign.<sup>[21]</sup> Moreover, SWNTs can be assembled in different morphologies, such as random-networked films,<sup>[6, 17, 22-24]</sup> horizontal-aligned arrays<sup>[15, 25]</sup> or hierarchical architectures<sup>[26-28]</sup> for various applications ranging from structural electronics to integrated photonic systems. However, there is still plenty of room to improve the performance of the SWNT-based TCFs. Doping could increase the charge carrier density of SWNTs and eliminate the Schottky barrier between metallic and semiconducting SWNTs, and thus could further improve the electrical conductivity of the SWNT films.<sup>[28]</sup> Unfortunately, because of the chemical inertness of the covalent-bonded graphitic surface, it is still a great challenge to achieve stable and satisfactory doping of SWNTs.

Strong oxidizing agents have been extensively investigated as effective *p*-type dopants for SWNTs, including inorganic redox agents such as  $\text{HNO}_3$ ,<sup>[24, 30-33]</sup>  $\text{H}_2\text{SO}_4$ ,<sup>[34-36]</sup>  $\text{SOCl}_2$ ,<sup>[37]</sup>  $\text{AuCl}_3$ <sup>[38-40]</sup> and  $\text{O}_3$ ,<sup>[41-43]</sup> as well as organic redox agents such as bis-(trifluoromethanesulfonyl)imide (TFSI)<sup>[44, 45]</sup> tetrafluorotetracyano-*p*-quinodimethane

(F<sub>4</sub>TCNQ),<sup>[29, 46]</sup> *etc.* However, the common disadvantage of these redox dopants is the instability in the ambient environment, which would cause the doping effect disappear quickly. Recently, metal oxides with low-lying work function are drawing increasing research interest because of their stability in the ambient. It has been reported that molybdenum oxide<sup>[3, 47-49]</sup> and tungsten oxide<sup>[50]</sup> with work function greater than 6 eV were effective *p*-type dopants for both SWNTs and graphene. Nevertheless, the metal-oxide based doping method usually requires high-temperature annealing processes (around 400 °C) to induce oxygen deficiency and nonstoichiometry, and thus realizes charge transfer from SWNTs to the metal oxide. The high-temperature annealing process makes it difficult for use on substrates with low working temperatures, especially the polymer-based flexible transparent substrates such as polydimethylsiloxane (PDMS)<sup>[51]</sup> and parylene<sup>[52]</sup>. Moreover, the deposition of the metal oxide needs to be carried out in a clean-room environment by vacuum evaporation or sputtering, which lacks scalability for practical applications.

Here we propose a room-temperature and scalable doping process for SWNT thin films by using drop-casting/spin-coating CuCl<sub>2</sub>/Cu(OH)<sub>2</sub> colloidal solid-state redox. The doping process demonstrated immediate efficacy and year-long stability in the ambient. The downshift of the Fermi level was confirmed by Raman and photoelectron yield spectroscopies, and the charge transfer mechanism was investigated x-ray photoelectron spectroscopy. The SWNT/Si solar cells<sup>[23, 53-64]</sup> serve as a good benchmark to evaluate the performance of the SWNT TCFs, of which the power conversion efficiencies (PCEs) almost solely depend on the performance of the SWNT films and the compatibility of the fabrication process. We applied the redox-functionalized SWNT (rf-SWNT) films to the SWNT/Si solar cells and observed an over 100% improvement of the PCE with year-long stability compared with the pristine SWNT/Si solar cells. The role of the CuCl<sub>2</sub>/Cu(OH)<sub>2</sub> redox was further revealed by temperature-dependent current density-voltage characteristics of the SWNT/Si solar cells.

## 2. Solid-State Redox Functionalization

The pristine SWNT films were prepared by aerosol chemical vapor deposition (CVD) method (see Experimental Method). **Figure 1a** shows the morphology of the random-networked SWNT film with optical transparency of 90% at the wavelength of 550 nm. The average bundle length of the SWNTs was *ca.* 9  $\mu\text{m}$ .<sup>[6]</sup> The redox colloidal solution was prepared by gradually adding 1 M NaOH aqueous solution to 0.1 M  $\text{CuCl}_2$  ethanol solution with magnetic stirring. The volume ratio of the two solutions was 1:2000. The obtained redox colloidal solution was then drop-cast/spin-coated on the dry-transferred SWNT film on a Si/SiO<sub>2</sub> substrate. The film was subsequently dried in the ambient to fully evaporate the solvent. The SEM image (Figure 1b) demonstrated that the redox was well attached to the SWNT bundles throughout the whole surface, owing to the excellent wettability of ethanol over SWNTs. The uniform redox attachment to the SWNTs could help with the elimination of the blind spots (less conductive area) in the thin film. The Raman spectra of the SWNT films before and after the  $\text{CuCl}_2/\text{Cu}(\text{OH})_2$  redox coating are compared in Figure 1c, using 532 nm laser excitation (Renishaw inVia). The as-synthesized SWNTs possessed very high degree of graphitization and crystallinity with G/D ratio over 30. The radial-breathing mode (RBM) band indicated an average SWNT diameter of *ca.* 2 nm. After the  $\text{CuCl}_2/\text{Cu}(\text{OH})_2$  redox coating, the significant decrease in the Raman intensity and the blue shift in the G and G' bands of the redox-functionalized SWNT (rf-SWNT) films demonstrated the *p*-type doping effect. In the meantime, the RBM could be hardly detected, owing to the loss of resonance enhancement in the rf-SWNT samples. The *p*-type doping signature of SWNTs was evidenced by RBM, G-band and G'-band in Raman.

The results of the UV-vis-NIR optical absorbance spectroscopy (Shimadzu UV-3150) further corroborated the *p*-type doping effect. As shown in Figure 1d, the first optical transition of the van Hove singularities ( $E_{11}^s$ ) of the rf-SWNTs was completely quenched. This is related to the suppression of inter-band optical absorption due to the shift of the Fermi level, which may be attributed to the charge transfer from SWNTs to the  $\text{CuCl}_2/\text{Cu}(\text{OH})_2$  redox. The

second optical transition of the van Hove singularities ( $E_{22}^S$ ) was also significantly suppressed. The  $E_{22}$  usually cannot be completely quenched because of the much higher electronic density of states (eDOS) below the  $E_{11}$ .<sup>[33, 65, 66]</sup> The absorption spectrum of CuCl<sub>2</sub>/Cu(OH)<sub>2</sub> redox drying on fused quartz substrate is given in Supporting Information **Figure S1** as a reference, which identified the sharp absorption peak at 2943 nm as CuCl<sub>2</sub>. The UV-vis-NIR absorption spectra indicated that the Fermi level of the rf-SWNTs may lie in between  $E_{11}^S$  and  $E_{22}^S$ . To accurately quantify the position of the Fermi level, we carried out the photoelectron yield spectroscopy (PYS, Riken Keiki) and Kelvin probe spectroscopy (ESA) on the SWNT films before and after the CuCl<sub>2</sub>/Cu(OH)<sub>2</sub> redox functionalization. To eliminate the effect of oxygen doping from the ambient, the pristine SWNT films were annealed at 300 °C for 2 hours with N<sub>2</sub> protection. The PYS results showed that the work function of the pristine SWNTs was 4.83 eV, while the work function of the rf-SWNT film was 5.06 eV. The PYS data was consistent with the result of the absorption spectra, which demonstrated the position of the Fermi level was between the  $E_{11}^S$  and  $E_{22}^S$  for the rf-SWNTs. The work function of the CuCl<sub>2</sub>/Cu(OH)<sub>2</sub> redox dried out on the Si/SiO<sub>2</sub> substrate was 6.10 eV. The low-lying work function of the CuCl<sub>2</sub>/Cu(OH)<sub>2</sub> redox induced spontaneous electron transfer from the SWNTs without any post-treatment such as annealing or other additional process.

Figure 1e shows the sheet resistance of the pristine SWNT film, the rf-SWNT film immediately after doping as well as the rf-SWNT film stored in the ambient for 12 months. The sheet resistance of the pristine SWNT film reduced by a factor of 4.4 after the redox doping process, from 306.9  $\Omega$  sq.<sup>-1</sup> to 69.4  $\Omega$  sq.<sup>-1</sup>. In ambient condition for one year, the sheet resistance of the rf-SWNT film only slightly increased to 73.5  $\Omega$  sq.<sup>-1</sup>. Compared with the previously reported values<sup>[29]</sup>, this sets a record on the stability of the doping process for SWNTs. Therefore, in addition to the immediate efficacy of the process, the Cu-based redox-SWNT charge transfer system shows excellent stability in the ambient for a long period.

To investigate the mechanism of the doping effect, XPS was carried out to compare the Cu  $2p$   $3/2$  peak of the dried  $\text{CuCl}_2/\text{Cu}(\text{OH})_2$  redox and the rf-SWNTs on the Si/SiO<sub>2</sub> substrates, as shown in **Figure 2a** and **2b**, respectively. From the Gaussian curve fitting of the XPS spectrum of the dried  $\text{CuCl}_2/\text{Cu}(\text{OH})_2$  redox (**Figure 2a**), both the Cu (I) and Cu (II) peaks could be observed. This demonstrated the ease of Cu extracting the electrons from environmental hydrocarbons. According to Ellingham diagram,<sup>[67]</sup> the Gibbs free energy change required for the Cu (II) to Cu (I) transition is among the least of redox reactions at room temperature. The intensity of the Cu (II) was approximately 1.5 times higher than that of the Cu (I), indicating that the Cu (II) was still the majority. **Figure 2b** represents the XPS spectrum of the rf-SWNT film. The Cu (II) / Cu (I) ratio drastically changed to 0.5, demonstrating a three-fold decrease compared with the dried  $\text{CuCl}_2/\text{Cu}(\text{OH})_2$  redox. The reduction of the Cu (II) / Cu (I) ratio confirmed the instant charge transfer from the SWNTs to the  $\text{CuCl}_2/\text{Cu}(\text{OH})_2$  redox. On the other hand, the Cu (II) hydroxide underwent barely any changes in the intensity with slightly widened full width half maximum (FWHM). The lesser active Cu (II) hydroxide could realize persistent charge transfer effect on the SWNTs. The combined effect of  $\text{CuCl}_2$  and  $\text{Cu}(\text{OH})_2$  led to the immediate efficacy and long-time stability of the proposed redox functionalization process for SWNTs. The schematics of the  $\text{CuCl}_2/\text{Cu}(\text{OH})_2$  redox-SWNT charge transfer system are shown in **Figure 2c**. The Cu (II) in the  $\text{CuCl}_2/\text{Cu}(\text{OH})_2$  received an electron from the SWNT and was reduced to Cu (I), meanwhile the Fermi level of the SWNTs was shifted downward to the valence band.

### 3. Heterojunction Solar Cells

As the  $\text{CuCl}_2/\text{Cu}(\text{OH})_2$  redox functionalization could significantly decrease the sheet resistance and downshift the Fermi level of the SWNTs, the rf-SWNT film would serve as an efficient hole-transporting layer in a solar cell. We applied the rf-SWNT films to the SWNT/Si heterojunction solar cells. As shown in **Figure 3a**, the SWNT film was transferred onto the bare Si window surrounding with Pt electrode. The current density–voltage ( $J$ - $V$ )

curves of the pristine SWNT/Si solar cells and the rf-SWNT/Si solar cells were compared under  $100 \text{ mW cm}^{-2}$  AM 1.5G illumination and dark conditions, as shown in Figure 3b. The PCE of the pristine SWNT/Si solar cell was 6.6%. This value was smaller than our previous reported value<sup>[21]</sup> because of the thicker interfacial oxide layer resulted from the RCA treatment. After the  $\text{CuCl}_2/\text{Cu}(\text{OH})_2$  redox functionalization process, the PCE of the rf-SWNT/Si heterojunction solar cell was increased by 115%, reaching the value of 13.77%. The open-circuit voltage ( $V_{\text{OC}}$ ), short-circuit current density ( $J_{\text{SC}}$ ) and fill factor (FF) were all significantly increased, with the  $V_{\text{OC}}$  increased from 458 mV to 547 mV, the  $J_{\text{SC}}$  increased from 29.3 to 35.2  $\text{mA cm}^{-2}$  and the FF increased from 49.2% to 71.6%. The quantitative results of the  $J$ - $V$  characterization are given in Table 1. The average values and standard deviations of PCE, FF,  $J_{\text{SC}}$  and  $V_{\text{OC}}$  of 20 SWNT/Si solar cells with and without redox functionalization are given in Supporting Information Figure S2 and Table S1. Both the pristine SWNT/Si solar cells and the rf-SWNT/Si solar cells have very high reproducibility; in fact, Table S1 shows the redox functionalization process could slightly increase the reproducibility of SWNT/Si solar cells.

The significant improvement of the  $V_{\text{OC}}$  and FF can be attributed to the combined effect of the downshift of the Fermi level and the five-fold decrease of the sheet resistance of the rf-SWNTs compared with the pristine SWNTs, per the PYS-Kelvin probe microscopy and four-point probe measurement. The strong charge transfer behavior between the  $\text{CuCl}_2/\text{Cu}(\text{OH})_2$  redox and the SWNTs resulted in the degenerate doping effect on the rf-SWNTs which served as an inversion layer on the crystalline surface of the  $n$ -type Si. To study the mechanism of the increase of  $J_{\text{SC}}$ , we carried out UV-vis-NIR reflectance spectroscopy on the pristine SWNT/Si solar cell and the rf-SWNT/Si solar cell, using bare Si substrate as a comparison group. As shown in Figure 3c, the pristine SWNT/Si solar cell exhibited similar reflectance with bare-Si substrate, with the integrated reflectance over the whole measurement range of 30.4%. The high reflectance of the bare Si substrate in the UV range was suppressed by the

strong  $\pi$  plasmon of SWNTs. The integrated reflectance over the whole measurement range of the rf-SWNT/Si solar cell was only 15.4%, which was 50% lower than that of the pristine SWNT/Si solar cell. Especially in the photon energy range larger than 1.1 eV which can be utilized for the SWNT/Si solar cell, there was an even larger degree of reduction in the reflectance. The antireflection effect of the  $\text{CuCl}_2/\text{Cu}(\text{OH})_2$  redox coating contributed to the increase of  $J_{\text{SC}}$ . A significant increase in the external quantum efficiency (EQE) was observed (Supporting Information **Figure S4**). For the rf-SWNT/Si solar cell, the EQE higher than 90% was achieved in the range of 500 nm to 700 nm wavelength, corresponding to the lowest reflectivity in the same wavelength range. The reflection spectra of the  $\text{CuCl}_2/\text{Cu}(\text{OH})_2$  redox with different coating thicknesses were measured as shown in Supporting Information **Figure S3**. The shift of the photon energy (wavelength) with minimal reflectance illustrated that the antireflection effect was attributed to the destructive interference originated from the different refractive indices between the redox coating and the Si substrate. The simultaneous and remarkable improvement of the  $V_{\text{OC}}$ ,  $J_{\text{SC}}$  and FF of the SWNT/Si heterojunction solar cell was realized by one-step process of drop-casting  $\text{CuCl}_2/\text{Cu}(\text{OH})_2$  redox colloidal solution. Based on the benchmark study using the SWNT/Si solar cells, the rf-SWNTs multifunctional transparent conductive film is very promising for applications in other types of photovoltaic devices, such as organic or perovskite solar cell, as well as various optoelectronic devices.

The degradation of PCE over a short period of time is still a severe issue hindering the large-scale practical applications of the SWNT/Si solar cells. The PCE of the SWNT/Si solar cells reported so far could decrease up to 50% after being exposed in air within one hour, and even with protection, the PCE still degraded by 20%.<sup>[71-73]</sup> We tested the stability of the rf-SWNT/Si solar cells in the ambient and compared with the  $\text{HNO}_3$ -doped SWNT/Si solar cells. As shown in Figure 3d, the  $J$ - $V$  characteristics of the rf-SWNT/Si solar cells barely went through any changes after one-year exposure in the ambient. In fact, the PCE of the rf-SWNT/Si solar cells slightly increased from 13.77% to 14.09%, demonstrating the persistent

charge transfer between the SWNTs and the  $\text{CuCl}_2/\text{Cu}(\text{OH})_2$  redox. The slight improvement is likely resulted from the better contact between the SWNTs and the substrate, which was evidenced by the reduced system series resistance (using equivalent circuit model shown later) from 10.5 to 9.0  $\Omega$  after one-year exposure in the ambient. This is the highest air-stable PCE reported so far among the SWNT/Si solar cells. As a comparison group, after applying  $\text{HNO}_3$  doping, the PCE of the SWNT/Si solar cell was increased to 10.17% immediately after the drying out the  $\text{HNO}_3$ . However, the PCE dropped quickly afterwards, and eventually stabilized at 6.41% after two-month exposure in the ambient, which was almost the same as the original value of the pristine SWNT/Si solar cell. The disappearance of the doping effect on the PCE is attributed to the versatility of  $\text{HNO}_3$  in the ambient environment, resulting in the complete evaporation of  $\text{HNO}_3$ . The key of the record-long stability of the  $\text{CuCl}_2/\text{Cu}(\text{OH})_2$  redox functionalization lies in the  $\text{Cu}(\text{OH})_2$  which is the resource for constant doping, while the  $\text{CuCl}_2$  provides immediate efficacy of the charge transfer effect on the SWNTs.

The interfacial oxide layer between the nanocarbon materials and silicon substrate played an important role in improving solar cell performance and investigating the mechanism of such kind of solar cells. Song *et al*<sup>[69]</sup> and Jia *et al*<sup>[74]</sup> found that the optimal thickness of the interfacial oxide layer could be obtained through exposing the SWNT/Si solar cell in air for several days. Previously we found that the RCA treatment could effectively thicken the interfacial oxide layer, which provided a powerful tool to tune the interfacial oxide thickness in a wider range.<sup>[23]</sup> Figure 3e compares the  $J$ - $V$  characteristics of the pristine and rf-SWNT/Si solar cells with different RCA treatment time. The silicon substrates were soaked in the RCA solution for 3 s, 1 min, 2 min and 3 min before the deposition of electrodes. The oxide growth rate is proportional to the inversed time and the oxide thickness saturates after 3 min treatment, reaching an oxide thickness of 13 – 15  $\text{\AA}$ .<sup>[75-77]</sup> The pristine SWNT/Si solar cell with RCA treatment of 3 s exhibited the highest PCE among all the pristine ones, reaching 9%. With the increase of the soaking time in the RCA solution, both the  $V_{\text{OC}}$  and FF decreased remarkably,

resulting in a severe degradation of the solar cell performance. In general, compared with the pristine SWNT/Si solar cells, all the rf-SWNT/Si solar cells with different treatment time ranging from 3 s to 3 min showed improvement in terms of  $V_{OC}$ ,  $J_{SC}$  and FF. However, the improvement was almost negligible for the device with 3 s RCA treatment (see Supporting Information **Figure S5**). It could be attributed to the Fermi level pinning in the junction of SWNT and Si, and thus the photovoltage is independent of the work function of the SWNTs. The rf-SWNT/Si solar cell with RCA treatment of 2 min showed the highest PCE of 13.77%, while its pristine counterpart showed PCE of 6.6%. Drop-casting the redox solution on the pristine SWNT/Si solar cell with RCA treatment of 3 min resulted in an even larger degree of improvement in the PCE, *i.e.* 148%. However, the PCE of the rf-SWNT/Si solar cell with 3 min RCA treatment was still lower than that with 2 min RCA treatment, owing to the excessively thickened interfacial oxide layer. We also noticed similar trend of the FFs for both the pristine SWNT/Si solar cell and the rf-SWNT/Si solar cell. The increase of the interfacial oxide layer in Schottky-junction solar cells could separate the metallic or degenerately doped semiconductor layer from the moderately doped semiconductor part, and thus help unpin the Fermi level by reducing the surface states. On the other hand, the increase of interfacial oxide layer would also make it more difficult for the tunneling of charge carriers.

To investigate the role of the  $CuCl_2/Cu(OH)_2$  redox on the improvement of the SWNT/Si solar cells, we performed  $J$ - $V$  characteristic tests at different operating temperatures under the dark and AM1.5G conditions. The pristine SWNT/Si solar cell with 3 s RCA treatment, which has the highest PCE among all the pristine ones, was compared with the optimal rf-SWNT/Si solar cell with 2 min RCA treatment. **Figure 4a** and **4b** show the  $J$ - $V$  characteristics measured under AM1.5G illumination of the pristine SWNT/Si solar cell and the rf-SWNT/Si solar cell, respectively, at the operating temperatures ranging from 298 K to 368 K. Their logarithmic  $J$ - $V$  characteristics measured under the dark condition are given in the insets of **Figure 4a** and **4b**. The experimental  $J$ - $V$  characteristics are fitted using the diode equation (Equation 1)

$$J = J_{SC} - J_0 \exp\left[\frac{q(V + JR_S)}{nkT}\right] - \frac{V + JR_S}{R_{SH}} \quad (1)$$

where  $kT/q$  is the thermal voltage, the ideality factor  $n$  is derived from the slope of the linear regime of the  $J$ - $V$  curve under the dark condition, and the dark saturation current density  $J_0$ , series resistance  $R_S$  as well as the shunt resistance  $R_{SH}$  were extracted by curve fitting. As shown in the Supporting Information **Figure S2**, the  $J$ - $V$  characteristics of both the pristine and rf-SWNT/Si solar cells at all the test temperatures could be well fitted using Equation (1). As the  $R_{SH}$  is sufficiently large, under the open-circuit condition, we could derive the relationship between the  $J_{SC}$  and  $V_{OC}$  from Equation (1)

$$J_{SC} = J_0 \exp\left(\frac{qV_{OC}}{nkT}\right) = J_{00} \exp\left(\frac{qV_{OC}}{nkT}\right) \exp\left(-\frac{E_a}{nkT}\right) \quad (2)$$

where  $J_{00}$  is the temperature-independent pre-factor and  $E_a$  is the activation energy. It can be observed from Equation (2) that the dark saturation current density ( $J_0$ ) is of substantial importance, as  $V_{OC}$  is inversely proportional to  $J_0$ . Previous research found that  $J_0$  was dependent on the operating temperature and activation energy  $E_a$  at the heterojunction interface.<sup>[78-80]</sup> The  $E_a$  is essentially the band offset between the two materials in the junction, which could be used to distinguish the recombination mechanism. The value of  $E_a$  could be obtained from linear fitting to the plot of the corrected saturation current density  $n \times \ln(J_0)$  versus the inversed thermal energy  $1/kT$ , as shown in Figure 4c. For the rf-SWNT/Si solar cell with 2 min RCA treatment, the  $E_a$  was *ca.* 1.02 eV which was close to the bandgap of the silicon  $E_{g-silicon}$ , *i.e.* 1.15 eV. The good matching between  $E_a$  and  $E_{g-silicon}$  indicated that the bulk recombination regime<sup>[80-82]</sup> (Shockley-Reed-Hall recombination) on the silicon side was dominant. While for the pristine SWNT/Si solar cell with 3 s RCA treatment, the  $E_a$  reduced to 0.575 eV, which was half of the  $E_{g-silicon}$ . This strongly suggested the occurrence of Fermi level pinning<sup>[80]</sup> in the middle of Si bandgap, demonstrating interfacial recombination at the

SWNT and Si heterojunction. The analysis of  $E_a$  could also explain that, for the SWNT/Si solar cell with 3 s RCA treatment, even after the  $\text{CuCl}_2/\text{Cu}(\text{OH})_2$  redox functionalization process, there was almost no improvement in the  $V_{OC}$  and PCE. The existence of the native oxide layer between SWNTs and Si was critical to unpin the Fermi level, and the role of the  $\text{CuCl}_2/\text{Cu}(\text{OH})_2$  redox was to downshift the Fermi level and make it possible for the tunneling of charge carriers. Figure 4d shows the relationship between the series resistance and the operating temperature for the pristine SWNT/Si solar cell with 3 s RCA treatment and the rf-SWNT/Si solar cell with 2 min RCA treatment. At room temperature, the rf-SWNT/Si solar cell demonstrated much smaller  $R_S$  (5.62  $\Omega$ ) than the pristine SWNT/Si solar cell (16.8  $\Omega$ ), owing to the significant reduction of the sheet resistance achieved by the  $\text{CuCl}_2/\text{Cu}(\text{OH})_2$  redox functionalization process. It was worth mentioning that the  $R_S$  for the pristine SWNT/Si solar cell did not increase with the operating temperature. This was attributed to that the temperature-induced recombination was neutralized by thermally induced flow of charge carriers (tunneling) through the Schottky barrier.

### 3. Conclusion

In summary, we have demonstrated a facile redox functionalization process for SWNTs with immediate efficacy and long-time stability in the ambient environment. We have achieved the PCE value of 14.09% with more than one-year stability in air by employing the redox functionalization process on the SWNT/Si solar cells. This study opens up possibility for a new paradigm of room-temperature and scalable doping process for SWNTs, and paves the way for wide-range applications of SWNT-based multifunctional transparent conductive films. The record high and stable PCE of the SWNT/Si solar cells using the redox functionalization process lays the cornerstone for use in other photovoltaic devices such as organic and perovskite solar cells.

### 4. Experimental Section

*Preparation of SWNT Films:* The SWNT films were synthesized by the aerosol floating catalyst CVD method. Ferrocene vapor was thermally decomposed in the reactor at 880 °C. The SWNTs were grown on the decomposed Fe catalyst using carbon monoxide (4 L min<sup>-1</sup>) as feedstock. Microporous filters were used to collect the as-synthesized SWNTs to form thin films. The transparency of the SWNT films was controlled by changing the time of collection. The collected SWNT films can be transferred on the arbitrary substrates through the dry transfer method.

*Fabrication of SWNT/Si Solar Cells:* The SWNT/Si solar cell was fabricated by dry-transferring the SWNT film onto a 3 mm × 3 mm *n*-type Si contact window and surrounding electrodes. The *n*-type Si (SUMCO Inc.) has the resistivity of  $10 \pm 2.5 \Omega \cdot \text{cm}$  with the doping concentration of  $\sim 10^{15} \text{ cm}^{-3}$ . The *n*-type Si substrate was consequentially treated with RCA1 (H<sub>2</sub>O : NH<sub>4</sub>OH : H<sub>2</sub>O<sub>2</sub> = 5 : 1 : 1), 5 M NaOH and RCA2 (H<sub>2</sub>O : HCl : H<sub>2</sub>O<sub>2</sub> = 5 : 1 : 1) solution for 10 min, 40 min and 3 s, respectively, to remove contaminations and oxides. Metallic electrode and dielectric layer were sputtered onto the treated Si substrate with 3 mm × 3 mm physical mask arrays. The SWNT film was transferred using the dry-transfer method onto the top surface of the Si substrate after the removal of the physical masks. The back electrode was fabricated by RF-sputtering Ti (15 nm)/Pt (55 nm).

*Characterization.* The sheet resistance of SWNT films was measured by van de Pauw method using Agilent 4156C analyzer with a four-probe station. The XPS was measured by PHI 5000 VersaProbe. The performance of the SWNT/Si solar cells was measured by the Agilent 4156C analyzer. The 100 mW cm<sup>-2</sup> AM1.5G light source was provided by solar simulator model PEC-L01 from Peccell Technologies, Inc. The EQE was measured using Xe lamp with a monochromator and chopper as well as lock-in amplifier system (SR830).

### **Supporting Information**

Supporting Information is available from the Wiley Online Library or from the author.

### Acknowledgements

This work was supported by JSPS Grants-in-Aid for Scientific Research (Grant Nos. JP25107002, JP15H05760), Aalto University Energy Efficiency (AEF) research program project “MOPPI” and JST-EC DG RTD Coordinated Research Project ‘IRENA’ under the Strategic International Collaborative Research Program (JST-SICORP). Part of this work is based on results obtained from a project commissioned by the New Energy and Industrial Technology Development Organization (NEDO). K.C. acknowledges the JSPS Grant-in-Aid for Young Scientists (15K17983).

Received: ((will be filled in by the editorial staff))

Revised: ((will be filled in by the editorial staff))

Published online: ((will be filled in by the editorial staff))

### References

- [1] D. Bi, C. Yi, J. Luo, J.-D. Décoppet, F. Zhang, Shaik M. Zakeeruddin, X. Li, A. Hagfeldt, M. Grätzel, *Nat. Energy* **2016**, *1*, 16142.
- [2] S. N. Habisreutinger, T. Leijtens, G. E. Eperon, S. D. Stranks, R. J. Nicholas, H. J. Snaith, *Nano Lett.* **2014**, *14*, 5561.
- [3] I. Jeon, K. Cui, T. Chiba, A. Anisimov, A. G. Nasibulin, E. I. Kauppinen, S. Maruyama, Y. Matsuo, *J. Am. Chem. Soc.* **2015**, *137*, 7982.
- [4] D. R. Barbero, S. D. Stranks. *Adv. Mater.* **2016**, *28*, 9668.
- [5] N. Fukaya, D. Y. Kim, S. Kishimoto, S. Noda, Y. Ohno, *ACS Nano* **2014**, *8*, 3285.
- [6] A. G. Nasibulin, A. Kaskela, K. Mustonen, A. S. Anisimov, V. Ruiz, S. Kivistö, S. Rackauskas, M. Y. Timmermans, M. Pudas, B. Aitchison, M. Kauppinen, D. P. Brown, O. G. Okhotnikov, E. I. Kauppinen, *ACS Nano* **2011**, *5*, 3214.
- [7] B. J. Worfolk, S. C. Andrews, S. Park, J. Reinspach, N. Liu, M. F. Toney, S. C. B. Mannsfeld, Z. Bao, *Proc. Natl. Acad. Sci. U. S. A.* **2015**, *112*, 14138.
- [8] H. Wu, D. Kong, Z. Ruan, P.-C. Hsu, S. Wang, Z. Yu, T. J. Carney, L. Hu, S. Fan, Y. Cui, *Nat. Nanotechnol.* **2013**, *8*, 421.
- [9] Y. Yang, A. J. Heeger, *Appl. Phys. Lett.* **1994**, *64*, 1245.
- [10] D. Zhang, K. Ryu, X. Liu, E. Polikarpov, J. Ly, M. E. Tompson, C. Zhou, *Nano Lett.* **2006**, *6*, 1880.
- [11] W.-Y. Jin, R. T. Ginting, K.-J. Ko, J.-W. Kang, *Sci. Rep.* **2016**, *6*, 36475.
- [12] D. Kuzum, H. Takano, E. Shim, J. C. Reed, H. Juul, A. G. Richardson, J. de Vries, H. Bink, M. A. Dichter, T. H. Lucas, D. A. Coulter, E. Cubukcu, B. Litt, *Nat. Commun.* **2014**, *5*, 5259.
- [13] D.-W. Park, S. K. Brodnick, J. P. Ness, F. Atry, L. Krugner-Higby, A. Sandberg, S. Mikael, T. J. Richner, J. Novello, H. Kim, D.-H. Baek, J. Bong, S. T. Frye, S. Thongpang, K. I. Swanson, W. Lake, R. Pashaie, J. C. Williams, Z. Ma, *Nat. Protocols* **2016**, *11*, 2201.
- [14] D.-W. Park, A. A. Schendel, S. Mikael, S. K. Brodnick, T. J. Richner, J. P. Ness, M. R. Hayat, F. Atry, S. T. Frye, R. Pashaie, S. Thongpang, Z. Ma, J. C. Williams, *Nat. Commun.* **2014**, *5*, 5258.
- [15] X. He, W. Gao, L. Xie, B. Li, Q. Zhang, S. Lei, J. M. Robinson, E. H. Hároz, S. K. Doorn, W. Wang, R. Vajtai, P. M. Ajayan, W. W. Adams, R. H. Hauge, J. Kono, *Nat. Nanotechnol.* **2016**, *11*, 633.
- [16] D.-m. Sun, M. Y. Timmermans, Y. Tian, A. G. Nasibulin, E. I. Kauppinen, S. Kishimoto, T. Mizutani, Y. Ohno, *Nat. Nanotechnol.* **2011**, *6*, 156.
- [17] Z. Wu, Z. Chen, X. Du, J. M. Logan, J. Sippel, M. Nikolou, K. Kamaras, J. R. Reynolds, D. B. Tanner, A. F. Hebard, A. G. Rinzler, *Science* **2004**, *305*, 1273.

- [18] L. Yu, C. Shearer, J. Shapter, *Chem. Rev.* **2016**, *116*, 13413.
- [19] S. Wu, W. Cui, N. Aghdassi, T. Song, S. Duhm, S.-T. Lee, B. Sun, *Adv. Funct. Mater.* **2016**, *26*, 5035.
- [20] Y. Liu, Z. Zhang, Z. Xia, J. Zhang, F. Liang, Y. Li, T. Song, X. Yu, S.-T. Lee, B. Sun, *ACS Nano* **2016**, *10*, 704.
- [21] L. He, S. C. Tjong, *Mater. Sci. Eng. R: Rep.* **2016**, *109*, 1.
- [22] Q. Cao, J. A. Rogers, *Adv. Mater.* **2009**, *21*, 29.
- [23] K. Cui, A. S. Anisimov, T. Chiba, S. Fujii, H. Kataura, A. G. Nasibulin, S. Chiashi, E. I. Kauppinen, S. Maruyama, *J. Mater. Chem. A* **2014**, *2*, 11311.
- [24] H.-Z. Geng, K. K. Kim, K. P. So, Y. S. Lee, Y. Chang, Y. H. Lee, *J. Am. Chem. Soc.* **2007**, *129*, 7758.
- [25] Q. Cao, S.-j. Han, G. S. Tulevski, Y. Zhu, D. D. Lu, W. Haensch, *Nat. Nanotechnol.* **2013**, *8*, 180.
- [26] M. De Volder, S. H. Tawfick, S. J. Park, D. Copic, Z. Zhao, W. Lu, A. J. Hart, *Adv. Mater.* **2010**, *22*, 4384.
- [27] K. Cui, T. Chiba, S. Omiya, T. Thurakitseree, P. Zhao, S. Fujii, H. Kataura, E. Einarsson, S. Chiashi, S. Maruyama, *J. Phys. Chem. Lett.* **2013**, *4*, 2571.
- [28] G. Zhang, Y. Song, H. Zhang, J. Xu, H. Duan, J. Liu, *Adv. Funct. Mater.* **2016**, *26*, 3012.
- [29] U. N. Maiti, W. J. Lee, J. M. Lee, Y. Oh, J. Y. Kim, J. E. Kim, J. Shim, T. H. Han, S. O. Kim, *Adv. Mater.* **2014**, *26*, 40.
- [30] J. L. Blackburn, T. M. Barnes, M. C. Beard, Y.-H. Kim, R. C. Tenent, T. J. McDonald, B. To, T. J. Coutts, M. J. Heben, *ACS Nano* **2008**, *2*, 1266.
- [31] R. Jackson, B. Domercq, R. Jain, B. Kippelen, S. Graham, *Adv. Funct. Mater.* **2008**, *18*, 2548.
- [32] P. N. Nirmalraj, P. E. Lyons, S. De, J. N. Coleman, J. J. Boland, *Nano Lett.* **2009**, *9*, 3890.
- [33] W. Zhou, J. Vavro, N. M. Nemes, J. E. Fischer, F. Borondics, K. Kamarás, D. B. Tanner, *Phys. Rev. B* **2005**, *71*, 205423.
- [34] B. S. Shim, J. Zhu, E. Jan, K. Critchley, N. A. Kotov, *ACS Nano* **2010**, *4*, 3725.
- [35] V. Skákalová, A. B. Kaiser, U. Dettlaff-Weglikowska, K. Hrnčariková, S. Roth, *J. Phys. Chem. B* **2005**, *109*, 7174.
- [36] P. Puech, T. Hu, A. Sapelkin, I. Gerber, V. Tishkova, E. Pavlenko, B. Levine, E. Flahaut, W. Bacsá, *Phys. Rev. B* **2012**, *85*, 205412.
- [37] Y. Wang, C.-a. Di, Y. Liu, H. Kajiura, S. Ye, L. Cao, D. Wei, H. Zhang, Y. Li, K. Noda, *Adv. Mater.* **2008**, *20*, 4442.
- [38] S. M. Kim, K. K. Kim, Y. W. Jo, M. H. Park, S. J. Chae, D. L. Duong, C. W. Yang, J. Kong, Y. H. Lee, *ACS Nano* **2011**, *5*, 1236.
- [39] A. Murat, I. Rungger, C. Jin, S. Sanvito, U. Schwingenschlögl, *J. Phys. Chem. C* **2014**, *118*, 3319.
- [40] K. K. Kim, J. J. Bae, H. K. Park, S. M. Kim, H.-Z. Geng, K. A. Park, H.-J. Shin, S.-M. Yoon, A. Benayad, J.-Y. Choi, Y. H. Lee, *J. Am. Chem. Soc.* **2008**, *130*, 12757.
- [41] J. Chen, R. Dhall, B. Hou, S. Yang, B. Wang, D. Kang, S. B. Cronin, *Appl. Phys. Lett.* **2016**, *109*, 153109.
- [42] Y. Miyauchi, M. Iwamura, S. Mouri, T. Kawazoe, M. Ohtsu, K. Matsuda, *Nat. Photonics* **2013**, *7*, 715.
- [43] P. P. Pal, T. Larionova, I. V. Anoshkin, H. Jiang, M. Nisula, A. A. Goryunkov, O. V. Tolochko, M. Karppinen, E. I. Kauppinen, A. G. Nasibulin, *J. Phys. Chem. C* **2015**, *119*, 27821.
- [44] K. K. Kim, S. M. Kim, Y. H. Lee, *Acc. Chem. Res.* **2016**, *49*, 390.
- [45] S. M. Kim, Y. W. Jo, K. K. Kim, D. L. Duong, H.-J. Shin, J. H. Han, J.-Y. Choi, J. Kong, Y. H. Lee, *ACS Nano* **2010**, *4*, 6998.
- [46] Y. Noshu, Y. Ohno, S. Kishimoto, T. Mizutani, *Nanotechnology* **2007**, *18*, 415202.
- [47] S. Esconjauregui, L. D'Arzié, Y. Guo, J. Yang, H. Sugime, S. Caneva, C. Cepek, J. Robertson, *ACS Nano* **2015**, *9*, 10422.

- [48] S. L. Hellstrom, M. Vosgueritchian, R. M. Stoltenberg, I. Irfan, M. Hammock, Y. B. Wang, C. Jia, X. Guo, Y. Gao, Z. Bao, *Nano Lett.* **2012**, *12*, 3574.
- [49] I. Jeon, T. Chiba, C. Delacou, Y. Guo, A. Kaskela, O. Reynaud, E. I. Kauppinen, S. Maruyama, Y. Matsuo, *Nano Lett.* **2015**, *15*, 6665.
- [50] L. Suriyasena Liyanage, X. Xu, G. Pitner, Z. Bao, H. S. P. Wong, *Nano Lett.* **2014**, *14*, 1884.
- [51] M. Kaltenbrunner, M. S. White, E. D. Głowacki, T. Sekitani, T. Someya, N. S. Sariciftci, S. Bauer, *Nat. Commun.* **2012**, *3*, 770.
- [52] J. Jean, A. Wang, V. Bulović, *Org. Elec.* **2016**, *31*, 120.
- [53] Y. Jia, A. Cao, X. Bai, Z. Li, L. Zhang, N. Guo, J. Wei, K. Wang, H. Zhu, D. Wu, P. M. Ajayan, *Nano Lett.* **2011**, *11*, 1901.
- [54] Y. Jia, P. Li, X. Gui, J. Wei, K. Wang, H. Zhu, D. Wu, L. Zhang, A. Cao, Y. Xu, *Appl. Phys. Lett.* **2011**, *98*, 133115.
- [55] Y. Jia, J. Wei, K. Wang, A. Cao, Q. Shu, X. Gui, Y. Zhu, D. Zhuang, G. Zhang, B. Ma, L. Wang, W. Liu, Z. Wang, J. Luo, D. Wu, *Adv. Mater.* **2008**, *20*, 4594.
- [56] Y. Jung, X. Li, N. K. Rajan, A. D. Taylor, M. A. Reed, *Nano Lett.* **2013**, *13*, 95.
- [57] X. Liu, X. W. Zhang, J. H. Meng, Z. G. Yin, L. Q. Zhang, H. L. Wang, J. L. Wu, *Appl. Phys. Lett.* **2015**, *106*, 233901.
- [58] X. Miao, S. Tongay, M. K. Petterson, K. Berke, A. G. Rinzler, B. R. Appleton, A. F. Hebard, *Nano Lett.* **2012**, *12*, 2745.
- [59] E. Shi, L. Zhang, Z. Li, P. Li, Y. Shang, Y. Jia, J. Wei, K. Wang, H. Zhu, D. Wu, S. Zhang, A. Cao, *Sci. Rep.* **2012**, *2*.
- [60] D. D. Tune, B. S. Flavel, J. S. Quinton, A. V. Ellis, J. G. Shapter, *ChemSusChem* **2013**, *6*, 320.
- [61] F. Wang, D. Kozawa, Y. Miyauchi, K. Hiraoka, S. Mouri, Y. Ohno, K. Matsuda, *Nat. Commun.* **2015**, *6*.
- [62] W. Xu, S. Wu, X. Li, M. Zou, L. Yang, Z. Zhang, J. Wei, S. Hu, Y. Li, A. Cao, *Adv. Energy Mater.* **2016**, *6*, 1600095.
- [63] J. M. Harris, R. J. Headrick, M. R. Semler, J. A. Fagan, M. Pasquali, E. K. Hobbie, *Nanoscale* **2016**, *8*, 7969.
- [64] X. Li, L. M. Guard, J. Jiang, K. Sakimoto, J.-S. Huang, J. Wu, J. Li, L. Yu, R. Pokhrel, G. W. Brudvig, S. Ismail-Beigi, N. Hazari, A. D. Taylor, *Nano Lett.* **2014**, *14*, 3388.
- [65] H. Shimotani, S. Tsuda, H. Yuan, Y. Yomogida, R. Moriya, T. Takenobu, K. Yanagi, Y. Iwasa, *Adv. Funct. Mater.* **2014**, *24*, 3305.
- [66] A. D. Avery, B. H. Zhou, J. Lee, E.-S. Lee, E. M. Miller, R. Ihly, D. Wesenberg, K. S. Mistry, S. L. Guillot, B. L. Zink, Y.-H. Kim, J. L. Blackburn, A. J. Ferguson, *Nat. Energy* **2016**, *1*, 16033.
- [67] P. Atkins, J. de Paula, *Physical Chemistry*. 8th ed.; Oxford University Press: Oxford, **2006**, Vol. 1., pp. 215.
- [68] E. Shi, H. Li, L. Yang, L. Zhang, Z. Li, P. Li, Y. Shang, S. Wu, X. Li, J. Wei, K. Wang, H. Zhu, D. Wu, Y. Fang, A. Cao, *Nano Lett.* **2013**, *13*, 1776.
- [69] Y. Song, X. Li, C. Mackin, X. Zhang, W. Fang, T. Palacios, H. Zhu, J. Kong, *Nano Lett.* **2015**, *15*, 2104.
- [70] E. Shi, L. Zhang, Z. Li, P. Li, Y. Shang, Y. Jia, J. Wei, K. Wang, H. Zhu, D. Wu, S. Zhang, A. Cao, *Sci. Rep.* **2012**, *2*, 884.
- [71] D. D. Tune, B. S. Flavel, R. Krupke, J. G. Shapter, *Adv. Energy Mater.* **2012**, *2*, 1043.
- [72] X. Li, Z. Lv, H. Zhu, *Adv. Mater.* **2015**, *27*, 6549.
- [73] Z. Zhang, L. Wei, X. Qin, Y. Li, *Nano Energy* **2015**, *15*, 490.
- [74] Y. Jia, A. Cao, F. Kang, P. Li, X. Gui, L. Zhang, E. Shi, J. Wei, K. Wang, H. Zhu, D. Wu, *Phys. Chem. Chem. Phys.* **2012**, *14*, 8391.
- [75] W. Kern, *J. Electrochem. Soc.*, **1990**, *137*, 1887.
- [76] K. Kobayashi, T. Susuki, S. Adachi, *Jpn. J. Appl. Phys.* **1994**, *33*, 15.
- [77] H. Anderson, *J. Electrochem. Soc.*, **1972**, *119*, 772.
- [78] T. Leijtens, J. Lim, J. Teuscher, T. Park, H. J. Snaith, *Adv. Mater.* **2013**, *25*, 3227.

- [79] Q. Cao, O. Gunawan, M. Copel, K. B. Reuter, S. J. Chey, V. R. Deline, D. B. Mitzi, *Adv. Energy Mater.* **2011**, *1*, 845.
- [80] K. Tvingstedt, C. Deibel, *Adv. Energy Mater.* **2016**, *6*, 1502230.
- [81] N. K. Elumalai, A. Uddin, *Energy Environ. Sci.* **2016**, *9*, 391.
- [82] M. D. Perez, C. Borek, S. R. Forrest, M. E. Thompson, *J. Am. Chem. Soc.* **2009**, *131*, 9281.

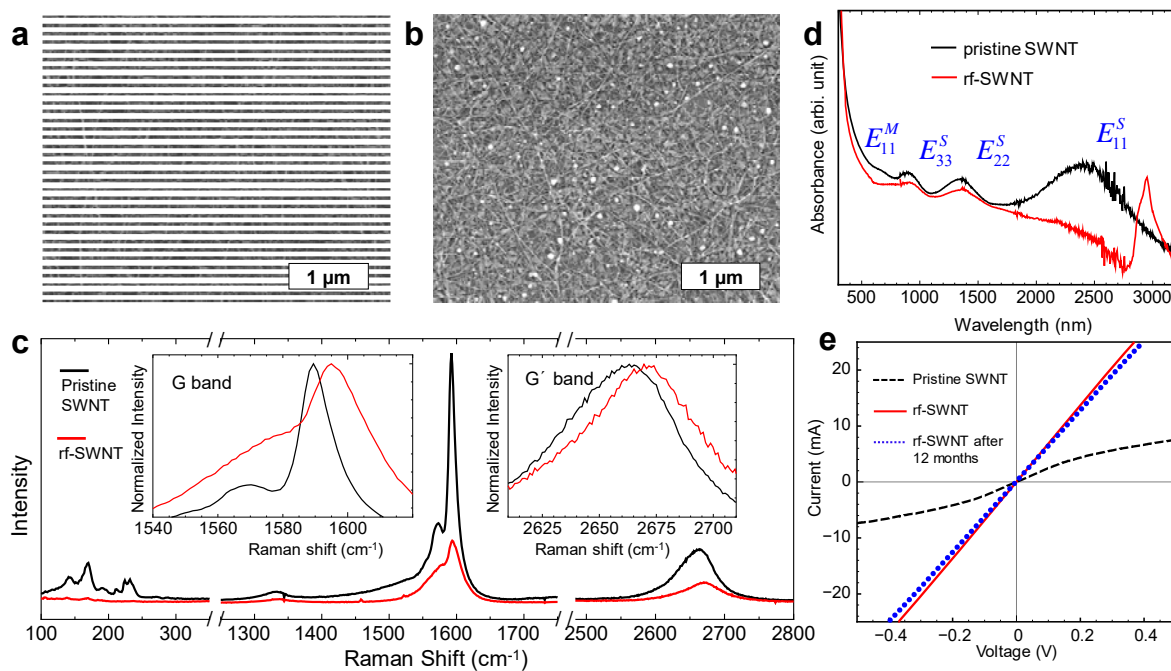


**Figure 1.** (a) SEM of the as-transferred SWNT film on the Si/SiO<sub>2</sub> substrate. (b) SEM of the rf-SWNT film on the Si/SiO<sub>2</sub> substrate. (c) Raman spectra of the as-transferred pristine SWNT film and the rf-SWNT film using 532 nm laser excitation. (d) UV-vis-NIR absorption spectra of the SWNT film before and after the Cu-based redox doping process. The peak at 2943 nm is from CuCl<sub>2</sub>. (e) Four-point probe measurement of sheet resistance of the pristine SWNT film, the immediate rf-SWNT film, as well as the rf-SWNT film stored in air for a year.

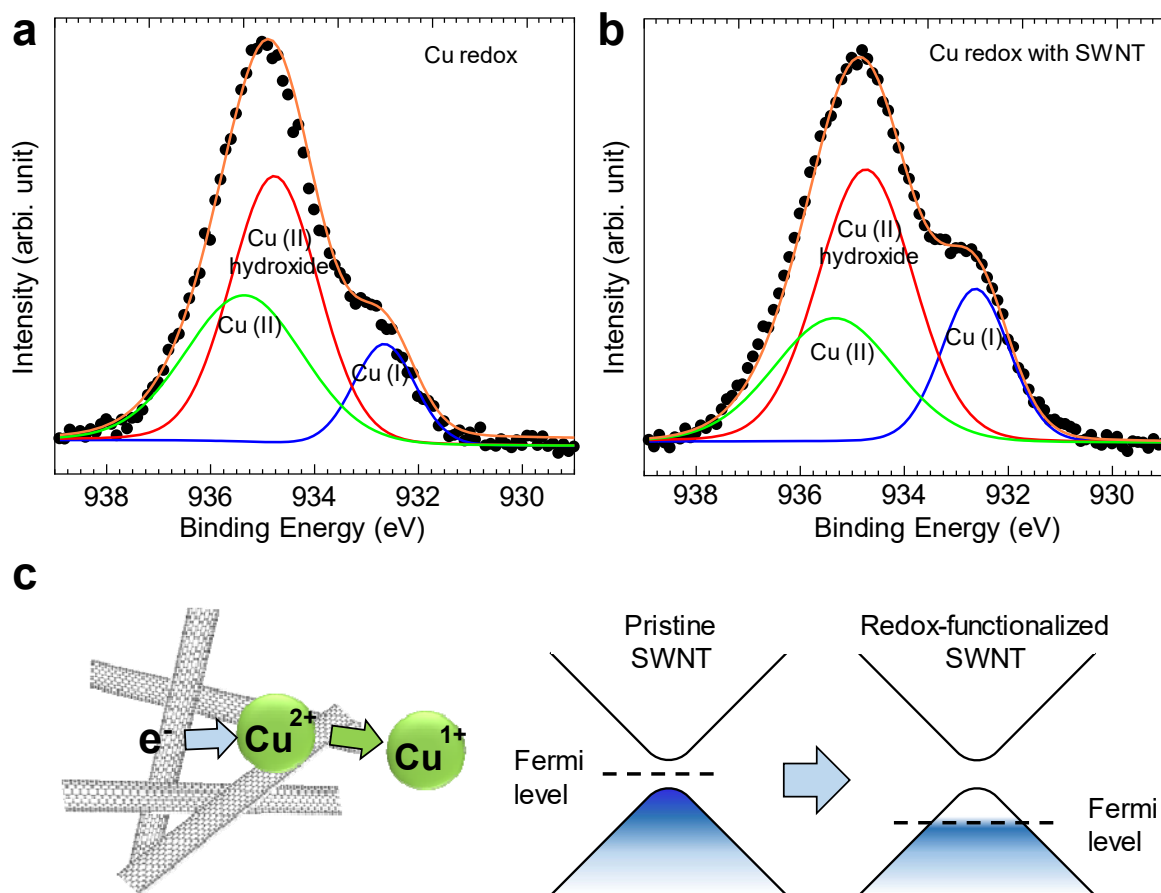


**Figure 2.** XPS spectra of (a) the CuCl<sub>2</sub>/Cu(OH)<sub>2</sub> redox dried on the Si/SiO<sub>2</sub> substrate and (b) the redox-functionalized SWNT film. (c) Schematics of the CuCl<sub>2</sub>/Cu(OH)<sub>2</sub> redox-SWNT charge transfer system.

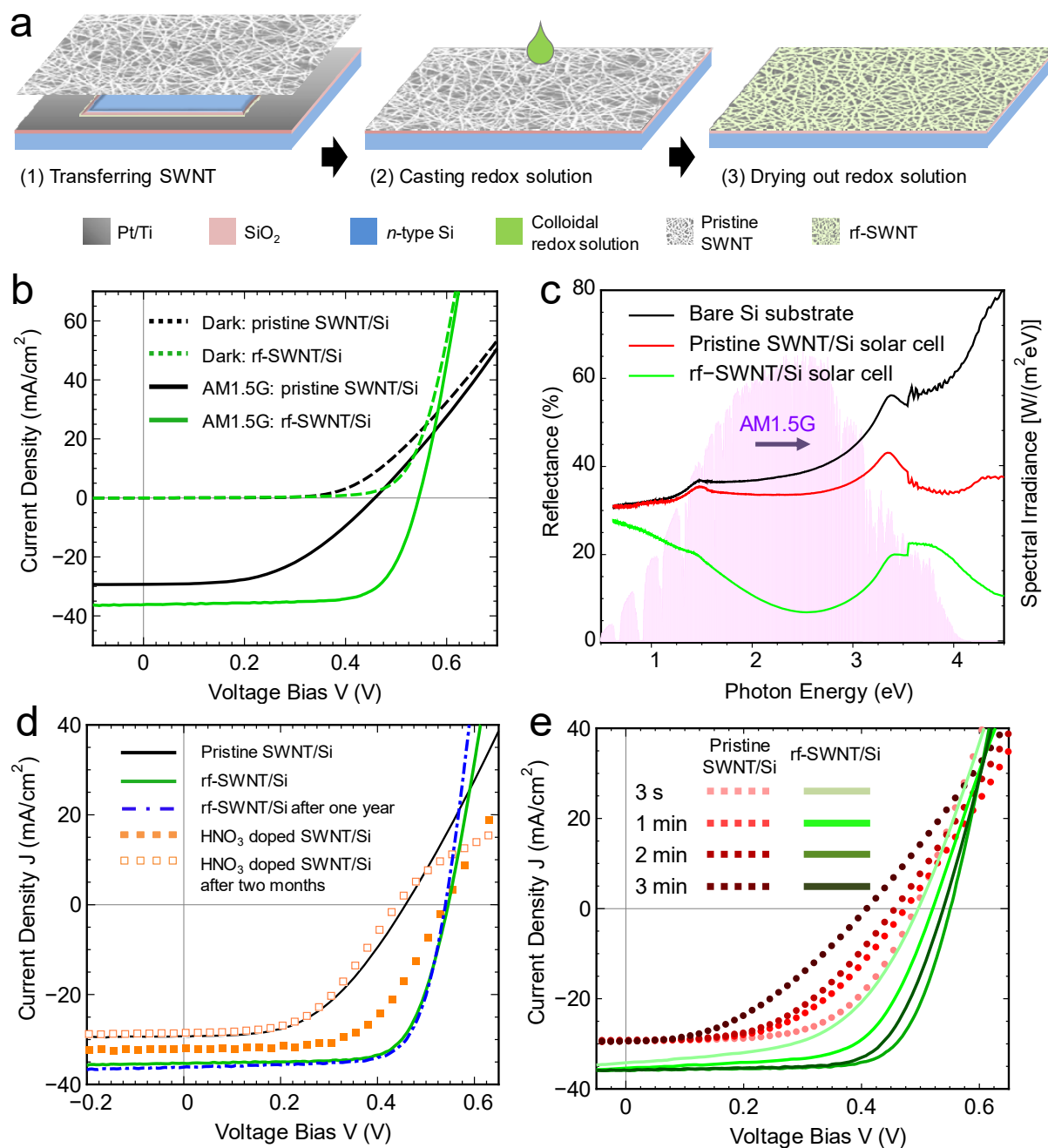


**Figure 3.** (a) Schematics of the  $\text{CuCl}_2/\text{Cu}(\text{OH})_2$  redox functionalization process for the SWNT/Si solar cells. (b)  $J$ - $V$  characteristics of the SWNT/Si solar cells before and after the  $\text{CuCl}_2/\text{Cu}(\text{OH})_2$  redox functionalization process. (c) UV-vis-NIR reflectance spectra of bare Si, the pristine SWNT film on bare Si and the rf-SWNT film on bare Si. (d) Comparison of the  $J$ - $V$  characteristics of the pristine SWNT-Si solar cell, the rf-SWNT/Si solar cell after fabrication and after one-year exposure in the ambient as well as the  $\text{HNO}_3$ -doped SWNT/Si solar cell after fabrication and after two-month exposure in the ambient. (e) Effect of varying RCA treatment time on the  $J$ - $V$  characteristics of the pristine SWNT/Si solar cells and the rf-SWNT/Si solar cells.

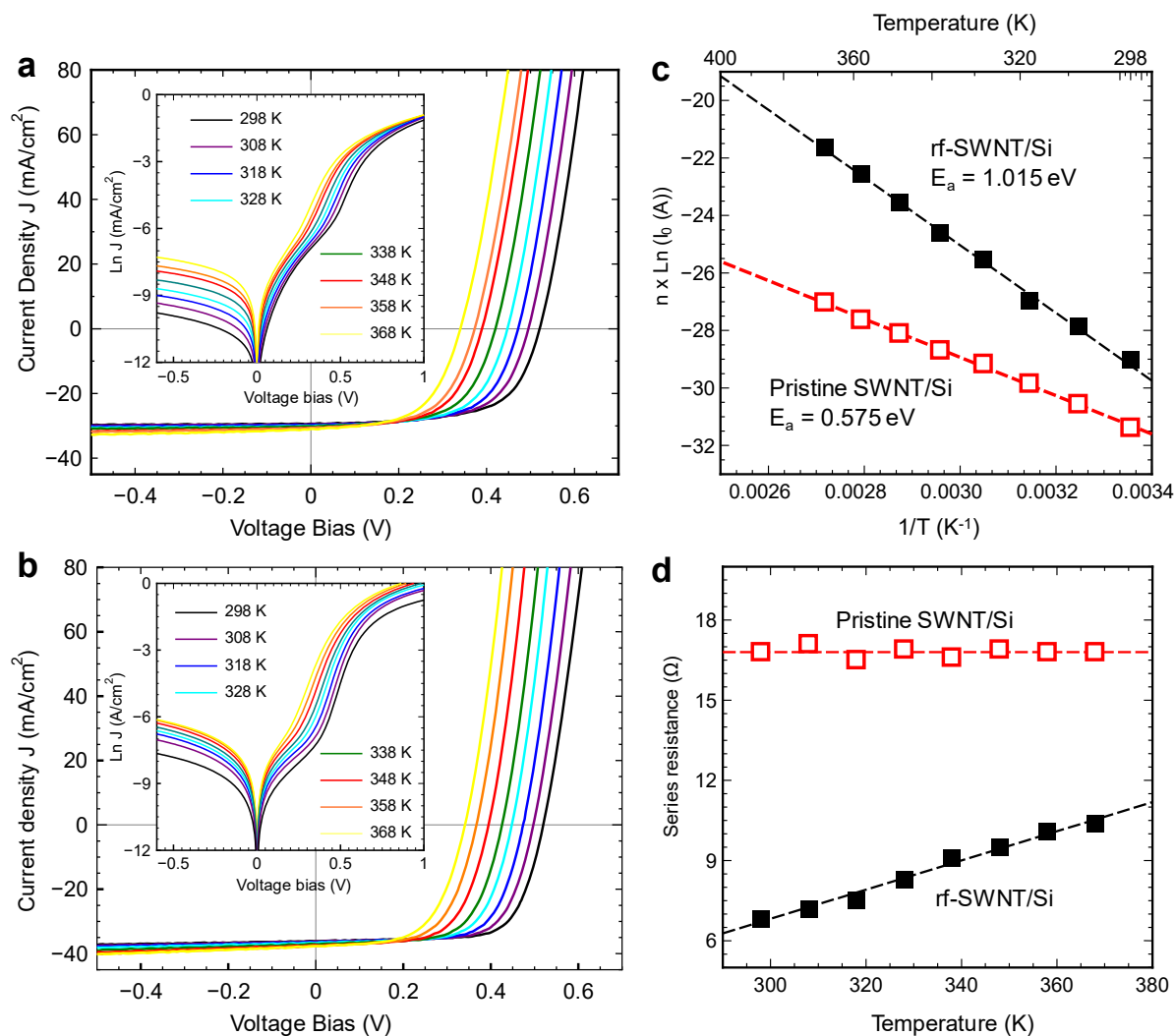


**Figure 4.**  $J$ - $V$  characteristics of the (a) pristine SWNT/Si solar cell with 3 s RCA treatment and (b) rf-SWNT/Si solar cell with 2 min RCA treatment measured at different operating temperatures from 298 K to 368 K under AM1.5G illumination condition. The insets were measured under dark condition. The variation of (c)  $n \times \ln(J_0)$  with the inversed operating temperature and (d) series resistance with the operating temperature for the pristine SWNT/Si solar cell with 3 s RCA treatment and the rf-SWNT/Si solar cell with 2 min RCA treatment.

**Table 1.** Power conversion efficiency (PCE), fill factor (FF), open-circuit voltage ( $V_{oc}$ ) and short-circuit current density ( $J_{sc}$ ) of the pristine SWNT/Si solar cell, the rf-SWNT/Si solar cell and the rf-SWNT/Si solar cell after one-year exposure in the ambient, compared with those of the  $HNO_3$ -SWNT/Si solar cell and the  $HNO_3$ -SWNT/Si solar cell after two-month exposure in the ambient.

	PCE (%)	FF (%)	$V_{oc}$ (mV)	$J_{sc}$ (mA cm <sup>-2</sup> )
Pristine SWNT/Si	6.59	49.2	458	29.3
rf-SWNT/Si	13.77	71.7	547	35.2
rf-SWNT/Si after one year	14.09	72.3	540	36.1
$HNO_3$ -SWNT/Si	10.17	59.1	539	31.9
$HNO_3$ -SWNT/Si after two months	6.41	50.6	443	28.6

## Table of Contents

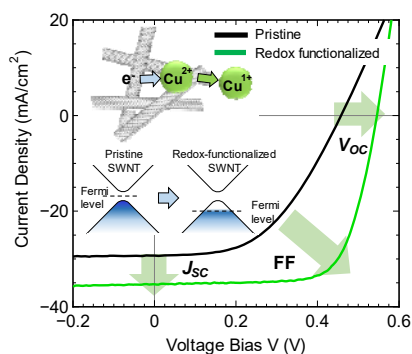
**A scalable and room-temperature solid-state redox functionalization process** for single-walled carbon nanotubes with instant efficacy and high stability is reported, with the sheet resistance reaching  $69.4 \Omega/\text{sq.}$  at 90% transparency without noticeable increase over 12 months. The redox functionalized films also serve as an antireflective layer for Si heterojunction solar cells, achieving the record-high air-stable power conversion efficiency of 14.09%.

**Keyword** solar cells, carbon nanotubes, functional coatings, doping

Kehang Cui,\* Yang Qian, Il Jeon, Anton Anisimov, Yutaka Matsuo, Esko I. Kauppinen, Shigeo Maruyama\*

**Title** Scalable and solid-state redox functionalization of transparent single-walled carbon nanotube films for highly efficient and stable solar cells

ToC figure ((55 mm broad  $\times$  50 mm high))



## Supporting Information

**Title** Scalable and solid-state redox functionalization of transparent single-walled carbon nanotube films for highly efficient and stable solar cells

*Kehang Cui,\* Yang Qian, Il Jeon, Anton Anisimov, Yutaka Matsuo, Esko I. Kauppinen, Shigeo Maruyama\**

### Table of Content

**Figure S1.** UV-vis-NIR absorption spectra of the SWNT film before and after the  $\text{CuCl}_2/\text{Cu}(\text{OH})_2$  redox doping process as well as the  $\text{CuCl}_2/\text{Cu}(\text{OH})_2$  redox coating on fused quartz substrate as a reference.

**Figure S2.** Current density-voltage ( $J$ - $V$ ) curves of 20 devices under AM1.5G 100  $\text{mW}/\text{cm}^2$  illumination. The curves in black denote the pristine SWNT/Si solar cells while those in green denote the redox functionalized SWNT/Si solar cells.

**Figure S3.** Reflection spectra of SWNT/Si devices with different thicknesses of redox coating with (a) photon energy and (b) wavelength as  $x$  axes.

**Figure S4.** External quantum efficiency of the pristine SWNT/Si solar cell and the rf-SWNT/Si solar cell.

**Figure S5.** Variations of the (a) power conversion efficiency (PCE), (b) open-circuit voltage ( $V_{\text{oc}}$ ) and (c) fill factor (FF) of the SWNT-Si solar cells before and after the redox functionalization with different RCA treatment time.

**Figure S6.** Curve fitting of the temperature-dependent current density-voltage ( $J$ - $V$ ) characteristics of (a) the pristine SWNT/Si solar cell with 3 s RCA treatment and (b) the rf-SWNT/Si solar cell with 2 min RCA treatment.

**Table S1.** Average values and standard deviations of power conversion efficiency (PCE), fill factor (FF), open-circuit voltage ( $V_{\text{oc}}$ ) and short-circuit current density ( $J_{\text{sc}}$ ) of 20 devices under AM1.5G 100  $\text{mW}/\text{cm}^2$  illumination with and without redox functionalization.

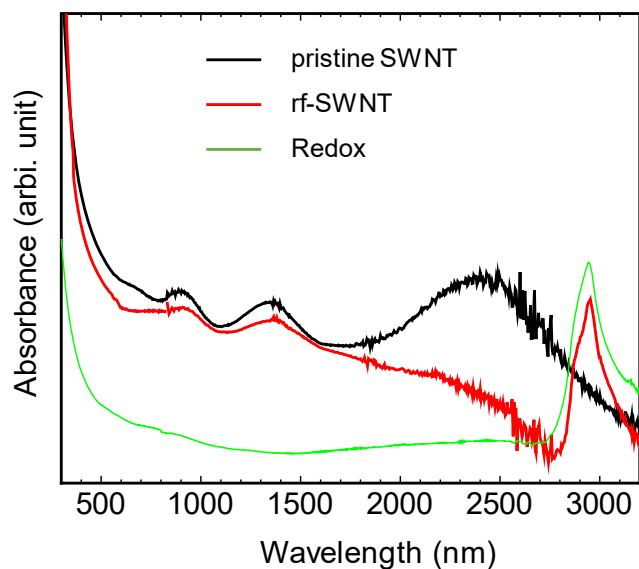


**Figure S1.** UV-vis-NIR absorption spectra of the SWNT film before and after the  $\text{CuCl}_2/\text{Cu}(\text{OH})_2$  redox doping process as well as the  $\text{CuCl}_2/\text{Cu}(\text{OH})_2$  redox coating on fused quartz substrate as a reference.

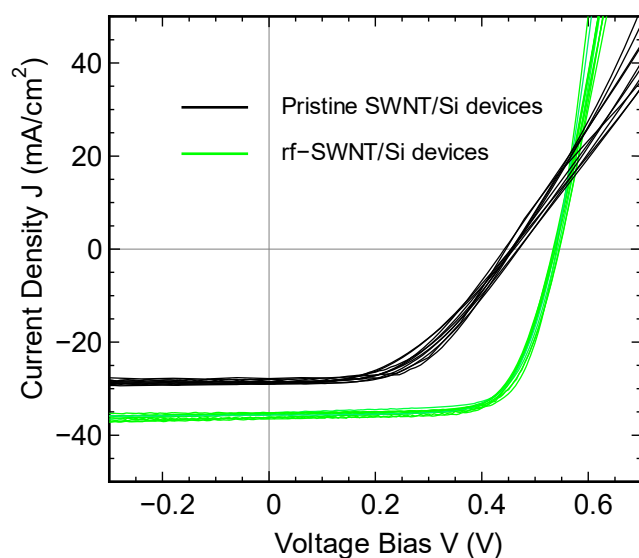


**Figure S2.** Current density-voltage ( $J$ - $V$ ) curves of 20 devices under AM1.5G 100  $\text{mW}/\text{cm}^2$  illumination. The curves in black denote the pristine SWNT/Si solar cells while those in green denote redox functionalized SWNT/Si solar cells.

**Table S1.** Average values and standard deviations of power conversion efficiency (PCE), fill factor (FF), open-circuit voltage ( $V_{oc}$ ) and short-circuit current density ( $J_{sc}$ ) of 20 devices under AM1.5G  $100 \text{ mW cm}^{-2}$  illumination with and without redox functionalization.

		PCE (%)	FF (%)	$V_{oc}$ (mV)	$J_{sc}$ ( $\text{mA cm}^{-2}$ )
pristine SWNT/Si solar cells	Avg.	6.43	49.2	455	28.6
	Std. Dev.	1.716	0.115	0.034	1.363
rf-SWNT/Si solar cells	Avg.	13.65	70.8	539	35.8
	Std. Dev.	0.817	0.025	0.011	1.867

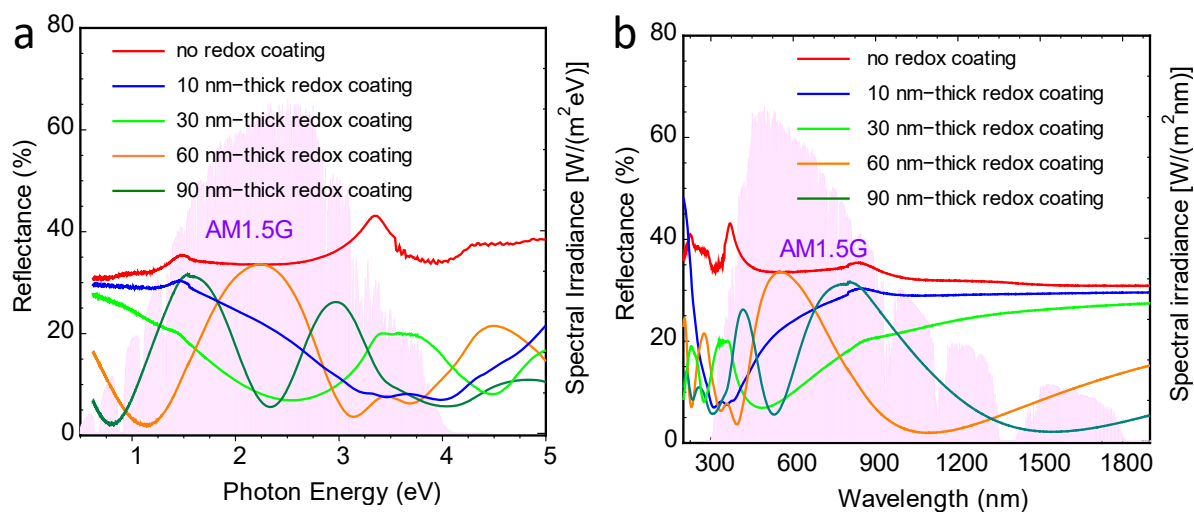


**Figure S3.** Reflection spectra of SWNT/Si devices with different thicknesses of redox coating with (a) photon energy and (b) wavelength as  $x$  axes.

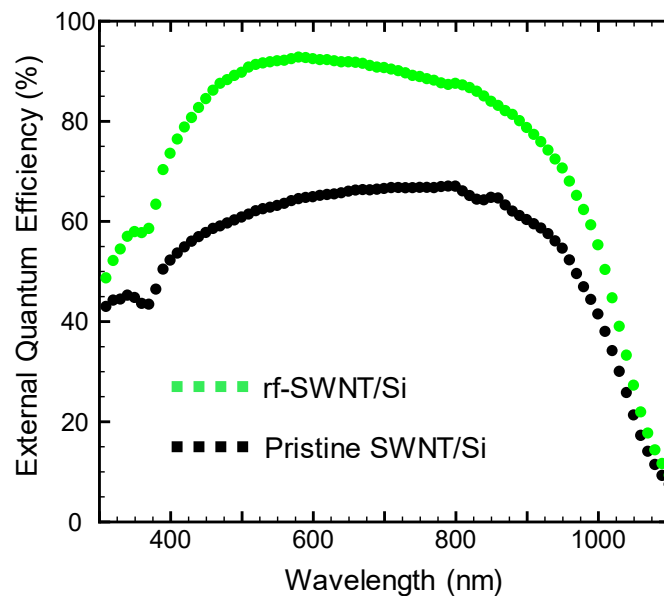


**Figure S4.** External quantum efficiency of the pristine SWNT/Si solar cell and rf-SWNT/Si solar cell.

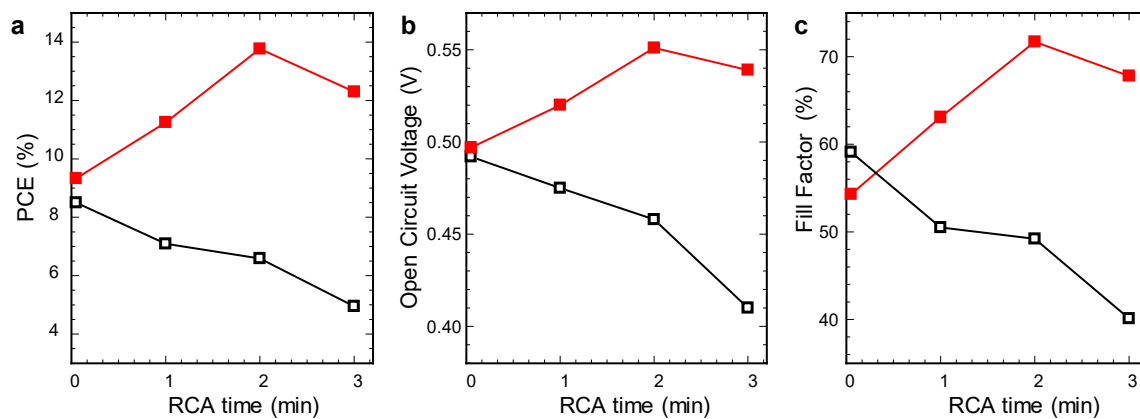


**Figure S5.** Variations of the (a) power conversion efficiency (PCE), (b) open-circuit voltage ( $V_{oc}$ ) and (c) fill factor (FF) of the SWNT-Si solar cells before and after the redox functionalization with different RCA treatment time.

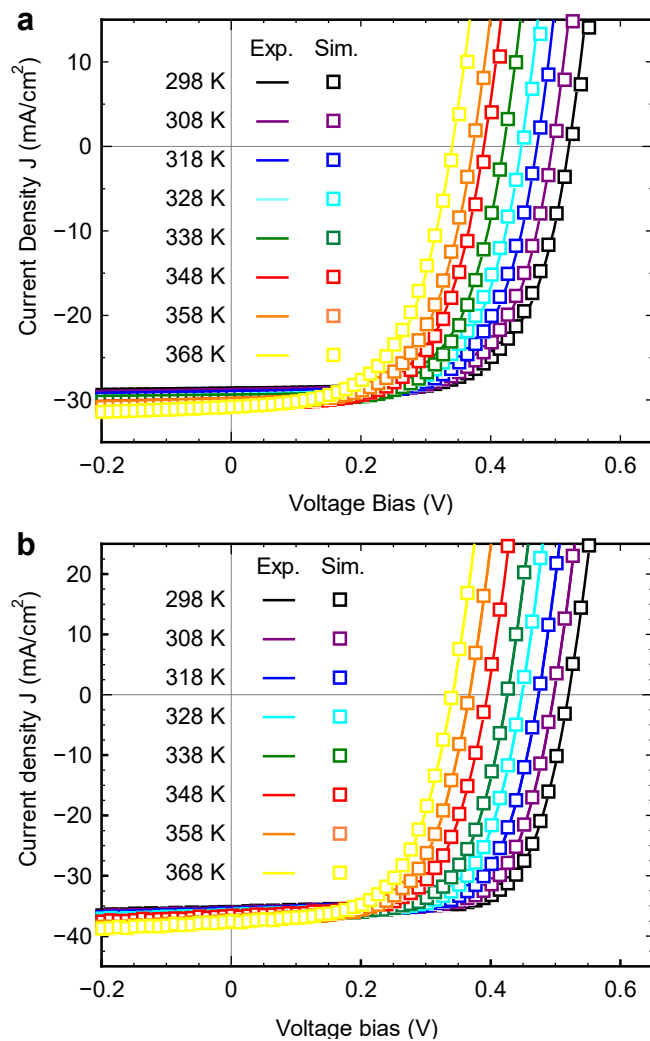


**Figure S6.** Curve fitting of the temperature-dependent current density-voltage ( $J$ - $V$ ) characteristics of (a) the pristine SWNT/Si solar cell with 3 s RCA treatment and (b) the rf-SWNT/Si solar cell with 2 min RCA treatment.